

# Exploring Cluster Physics with High-Resolution Sunyaev–Zel’dovich Effect Images and X-Ray Data: The Case of the Most X-Ray-Luminous Galaxy Cluster RX J1347–1145

Tetsu KITAYAMA,<sup>1</sup> Eiichiro KOMATSU,<sup>2,3</sup> Naomi OTA,<sup>4</sup> Takeshi KUWABARA,<sup>5</sup> Yasushi SUTO,<sup>5,6</sup>  
Kohji YOSHIKAWA,<sup>5</sup> Makoto HATTORI,<sup>7</sup> and Hiroshi MATSUO<sup>8</sup>

<sup>1</sup>*Department of Physics, Toho University, Funabashi, Chiba 274-8510*  
*kitayama@ph.sci.toho-u.ac.jp*

<sup>2</sup>*Department of Physics, Princeton University, Princeton, NJ 08544, USA*

<sup>3</sup>*Department of Astronomy, The University of Texas at Austin, Austin, TX 78712, USA*

<sup>4</sup>*Department of Physics, Tokyo Metropolitan University, Hachioji, Tokyo 192-0397*

<sup>5</sup>*Department of Physics, The University of Tokyo, Tokyo 113-0033*

<sup>6</sup>*Research Center for the Early Universe, The University of Tokyo, Tokyo 113-0033*

<sup>7</sup>*Astronomical Institute, Tohoku University, Aoba, Sendai 980-8578*

<sup>8</sup>*National Astronomical Observatory of Japan, Mitaka, Tokyo 181-8588*

(Received 2003 October 1; accepted 2003 November 25)

## Abstract

Foreseeing the era of high spatial resolution measurements of the Sunyaev–Zel’dovich effect (SZE) in clusters of galaxies, we present a prototype analysis of this sort combined with Chandra X-ray data. It is applied specifically to RX J1347–1145 at  $z = 0.451$ , the most X-ray-luminous galaxy cluster known, for which the highest resolution SZE and X-ray images are currently available. We demonstrate that the combined analysis yields a unique probe of complex structures in the intracluster medium, offering determinations of their temperature, density, and line-of-sight extent. For a subclump in RX J1347–1145, previously discovered in our SZE map, the temperature inferred after removing the foreground and background components is well in excess of 20 keV, indicating that the cluster has recently undergone a violent merger. Excluding the region around this subclump, the SZE signals in submillimeter to centimeter bands (350, 150, and 21 GHz) are all consistent with those expected from Chandra X-ray observations. We further present a temperature deprojection technique based on the SZE and X-ray images, without any knowledge of spatially resolved X-ray spectroscopy. The methodology presented here will be applicable to a statistical sample of clusters available in the future SZE surveys.

**Key words:** cosmology: observations – galaxies: clusters: individual (RX J1347–1145) – radio continuum: galaxies – submillimeter – X-rays: galaxies: clusters

## 1. Introduction

In the era of precision cosmology represented by the first-year WMAP data (Bennett et al. 2003; Spergel et al. 2003) among others, the scientific goals of studies on galaxy clusters are gradually shifting from the exploration of cosmology to investigations of cluster physics itself. For cosmological uses, clusters of galaxies are often assumed to be idealized spherical and homogeneous systems. Recent X-ray observations by Chandra and XMM-Newton, however, have revealed complex structures in a number of clusters, whose origins are still to be clarified (e.g. Markevitch et al. 2000, 2002; Peterson et al. 2003; Fabian et al. 2003). There has hence been an increasing need for accurate and reliable measurements of clusters at multi-wavelengths to further pursue studies on cluster physics.

The Sunyaev–Zel’dovich effect (SZE), the inverse Compton scattering of the cosmic microwave background by hot electrons, serves as yet another diagnosis of the intracluster medium (Sunyaev, Zel’dovich 1970, 1972; for

reviews see Rephaeli 1995; Birkinshaw 1999; Carlstrom et al. 2002). The intensity of the thermal SZE is proportional to the line-of-sight integral of the electron density times the temperature,  $\int n_e T_e dl$ , whereas that of the X-ray thermal Bremsstrahlung emission is proportional to  $\int n_e^2 T_e^{1/2} dl$ . The combination of the two thus yields independent measures of the density and temperature distributions, including the departure from spherical symmetry (Zaroubi et al. 1998; Hughes, Birkinshaw 1998; Yoshikawa, Suto 1999; Donahue, et al. 2003). In addition, it is still not easy to explore the nature of very hot ( $> 10$  keV) gas with X-ray facilities alone, as the energy band of X-ray spectrometers with sub-arcminute spatial resolution is currently limited to below 10 keV. The SZE has an advantage in resolving such hot gas even in distant clusters, given its linear dependence on  $T_e$  and its redshift independence (e.g. Rephaeli 1995). This is of particular importance in depicting violent activities in clusters, such as mergers and associated heating of the gas.

As of today, the spatial resolution of the majority of the SZE imaging observations is limited to arcminute scales, considerably lower than current X-ray observations ( $6''$  for XMM-Newton,  $0''.5$  for Chandra). This is largely due to the limited number of radio telescopes with sub-arcminute resolution in the range of wavelengths relevant to the SZE measurements. Controlling the systematics of such large telescopes to the sensitivity level required for the SZE imaging is also challenging. Interferometers are stable with carefully controlled systematics and have allowed high signal-to-noise ratio (S/N) imaging of the SZE (e.g., Jones et al. 1993; Carlstrom et al. 1996); the effective resolution ranges from  $15''$  to a few arcmin, with more S/N at the largest angular scales. A single-dish telescope with an array of detectors working at millimeter or submillimeter wavelengths is also a promising tool of the SZE imaging observations. It is highly plausible that an array with hundreds to thousands of bolometers, such as BOLOCAM (Glenn et al. 2003) and SCUBA-2 (Holland et al. 2003), will achieve an angular resolution of  $\sim 10''$  while retaining a wide field-of-view of  $\sim 10'$ .

Given the recent progress and numerous on-going plans of the SZE surveys, it is likely that future cluster data, especially at high redshifts, will be dominated by the SZE images and supplemented by the X-ray and optical follow-up observations. Therefore, we explore uses of the SZE data beyond the standard analysis done so far. An ideal and unique template for this purpose is provided by RX J1347–1145 at redshift  $z = 0.451$ , the most X-ray-luminous cluster of galaxies known (Schindler et al. 1995, 1997). This cluster is an exceptional target of high-resolution SZE observations for two reasons: 1) the central SZE intensity, characterized by the central  $y$ -parameter of  $y_0 \sim 10^{-3}$ , is more than twice as large as any other clusters observed to date, and 2) its compact size, characterized by an angular core radius of  $\theta_c \sim 7''$ , enables mapping within a relatively narrow field-of-view of existing facilities. A number of measurements have thus been carried out for this cluster (Komatsu et al. 1999, 2001; Pointecouteau et al. 1999, 2001; Reese et al. 2002).

We currently have SZE maps of RX J1347–1145 at three bands: an SZE *increment* map at 350 GHz with a spatial resolution of  $15''$  (Komatsu et al. 1999), and *decrement* maps at 150 GHz and 21 GHz with the resolutions  $13''$  and  $76''$ , respectively (Komatsu et al. 2001). In particular, our 150 GHz observation has achieved the highest resolution of the SZE images so far and revealed a complex substructure with enhanced decrement signals at  $\sim 20''$  off the X-ray center. The substructure was not visible in the previous ROSAT X-ray image (Schindler et al. 1997), indicating that it has a very high temperature that is far beyond the energy band of the ROSAT/HRI ( $< 2$  keV). This finding was subsequently confirmed by the Chandra observations with an emission-weighted temperature toward the substructure of  $18.0^{+2.7}_{-2.3}$  keV, much higher than the ambient temperature  $12.7 \pm 1$  keV (Allen et al. 2002). Based on their Keck spectroscopy of 47 member galaxies, Cohen and Kneib (2002) suggested that this cluster is undergoing a major merger. Indeed, this is a good demon-

stration that the SZE imaging observations provide an independent and powerful diagnosis of cluster physics.

In this paper, we combine our multi-band, high-resolution SZE images and the Chandra X-ray data of RX J1347–1145 to present a proto-type analysis that will continue to prove useful in the future. More specifically, we take into account radial temperature profile and non-sphericity of the intracluster gas to constrain the gas distribution and the cluster bulk motion. We also attempt to deproject temperature profile of the cluster on the basis of the SZE and X-ray surface brightness, without a knowledge of spatially resolved X-ray spectroscopy. Finally, we explore the physical nature of the high-temperature substructure and discuss its implications on the merger history and dynamical activities of the cluster.

Throughout the paper, we assume a standard set of cosmological parameters:  $\Omega_m = 0.27$ ,  $\Omega_\Lambda = 0.73$ , and  $h = 0.71$  (Spergel et al. 2003). In this cosmology, an angular size of  $1''$  corresponds to a physical size of 5.74 kpc at the cluster redshift  $z = 0.451$ . Unless stated otherwise, errors are given in  $1-\sigma$ .

## 2. Multi-Wavelength Data of RX J1347–1145

We describe below the observations and the data used in the present paper. The summary of the SZE data is presented in table 1.

### 2.1. Mapping Observations with SCUBA at 350 GHz

Our submillimeter mapping observations at 350 GHz were performed with the Sub-millimeter Common User Bolometer Array (SCUBA) (Holland et al. 1999), attached on the Nasmyth platform of the James-Clark-Maxwell Telescope (JCMT) in Hawaii. There are 37 and 91 bolometers at 350 and 650 GHz, respectively. The observations were carried out in 1998 and 1999. The first year data are published in Komatsu et al. (1999). The radial profile of the first year data clearly indicated an extended positive signal consistent with the SZE increment feature, and the fitted amplitude of the SZE matches the prediction of the X-ray data. While the azimuthally averaged radial profile had a reasonable S/N, the noise per each pixel of the map was too high to study the detailed morphology of the SZE, owing to poor weather. A typical zenith optical depth during the first year was  $\tau_{350} = 0.46 - 0.60$ , which corresponds to the “wet” condition at JCMT. The  $1-\sigma$  noise level averaged over the first year map was  $8.0$  mJy beam $^{-1}$ .

In order to improve on the S/N of the map, we performed additional observations on 1999 July 3 and 4. The weather condition of the second year was much better than that of the first year mentioned above. A typical zenith optical depth was  $\tau_{350} = 0.21$  on July 3 and  $\tau_{350} = 0.34$  on July 4. The  $1-\sigma$  noise level averaged over the second year map is  $6.4$  mJy beam $^{-1}$ , and that of the coadded map (shown in figure 1) is  $5.3$  mJy beam $^{-1}$ . We used the planet Uranus for the primary flux calibration and beam measurements. We also observed the planet Mars as a secondary flux calibrator, and checked the stability of the

**Table 1.** Summary of the SZE observations and the data used in the analysis.

Frequency	350 GHz	150 GHz	21 GHz
Facility	JCMT/SCUBA	Nobeyama/NOBA	Nobeyama/HEMT
Beam-size (FWHM)	15''	13''	76''
Field-of-view	2'.8 diameter	1'.9 × 1'.9	6'.0 × 6'.0
Average 1- $\sigma$ noise	5.3 mJy beam <sup>-1</sup>	1.6 mJy beam <sup>-1</sup>	0.9 mJy beam <sup>-1</sup>
Radial bins [arcsec]	10–20, 20–30, 30–40, 40–50, 50–65, 65–85	10–20, 20–30, 30–40, 40–50, 50–60, 60–75	60–110, 110–140, 140–170, 170–240

gain of the telescope. There was no significant gain variation during the observations; thus, the calibration error is dominated by the uncertainty in the flux of Uranus, which is less than 15%. The beam pattern was fitted by an elliptical Gaussian profile with axis sizes 15''.5 × 14''.3. For simplicity, however, we approximate the beam as a symmetric Gaussian whose size is the geometric mean of the elliptical fit, 14''.9. Since the beam-size of the first year map was 15''.2, we use 15'' as the effective FWHM beam-size of the coadded map. This approximation of the beam does not cause significant systematic errors compared to the instrumental noise level in the coadded map.

In both years, sky chopping was done in the azimuth direction with a length of 120''. The observations were made in the “jiggle” mode, where each bolometer samples 64 independent points on the sky separated by 3''.09. We have reduced the time-ordered data with the reduction tools in the SURF package (Jenness, Lightfoot 1998), following the standard data analysis pipeline. After deswiping, flat-fielding, extinction corrections, and the sky noise correction with REMSKY (Jenness et al. 1998), we have removed the spikes above 4- $\sigma$  in the time-ordered data using DESPIKE. The map-making routine, REBIN, allocates the reduced time-ordered data onto a rectangular grid with a Gaussian low-pass filtering. We choose 6'' as a nominal pixel size in the final map, because it is close to the Nyquist sampling at 350 GHz; thus, each pixel in the map is treated as being independent. The non-uniformity of noise in the map is taken into account explicitly.

Measurements of the SZE are in general difficult with SCUBA, except for very compact clusters, such as RX J1347–1145. Since the SZE signal is typically extended across the field-of-view ( $\sim 150''$  in diameter), a fraction of it will be lost by sky chopping. In the standard data analysis pipeline, REMSKY subtracts the average of some (if not all) selected bolometers from each bolometer upon each integration, further reducing the atmospheric noise as well as the SZE signal. Zemcov et al. (2003) proposed a way to partially resolve this problem; instead of subtracting the average flux, they subtract the signal correlated with that at 650 GHz upon each integration. Their method removes less SZE and is suitable for extended clusters, because the contribution of the SZE to the total flux is much smaller at 650 GHz than 350 GHz. It is, however, reported to increase noise by 15% compared to REMSKY. Considering both the advantages and disad-

vantages of the two methods, we adopted the standard pipeline mentioned above to yield a map with a better S/N for this particular cluster.

### 2.2. Mapping Observations with NOBA at 150 GHz

The Nobeyama Bolometer Array (NOBA, Kuno et al. 1993), mounted on the Nobeyama 45-m telescope in Japan, consists of 7 bolometers. Since the data we present here are exactly the same as those published in Komatsu et al. (2001), we outline our millimeter observations at 150 GHz only briefly, with particular emphasis on differences between the data reduction procedures of NOBA and SCUBA.

A notable difference between NOBA and SCUBA is that NOBA does not require chopping. The bolometers are read-out through six differential circuits between the central bolometer and the other six surrounding ones; the outputs are differential signals between the central bolometer and each of the six surrounding bolometers. The atmospheric noise is thus subtracted electronically rather than mechanically. In the map-making algorithm, the six differential outputs are used to reconstruct signals at the central bolometer. By rotating the array clockwise by 19°.1, a scan path yields seven equally-spaced lines with the separation of 5''.3, which determines the size of a pixel. We have performed two orthogonal raster scans ( $X$  and  $Y$  scans), each being 111''.3 wide and consisting of three parallel scans.

The baseline level varies from one scan to the other due to the atmospheric noise (the scanning effect). The scanning effect can be reduced by combining the two orthogonal raster scans. We use the so-called PLAITS method (Emerson, Gräve 1988), which reduces the scanning effect in Fourier space by suppressing the low-frequency modes that are aligned with the scan direction. The final map has the FWHM beam-size of 13'', the 1- $\sigma$  noise level of 1.6 mJy beam<sup>-1</sup>, and the field-of-view of 111''.3 × 111''.3.

### 2.3. Mapping Observations at 21 GHz

In addition to the high-resolution observations mentioned above, we also performed mapping observations at 21 GHz using the dual circular polarization HEMT amplifier mounted on the Nobeyama 45-m telescope. Details of the observations and the data are presented in Komatsu et al. (2001). The map has the FWHM beam-size of 76'', 1- $\sigma$  noise level of 0.9 mJy beam<sup>-1</sup>, and field-of-view of

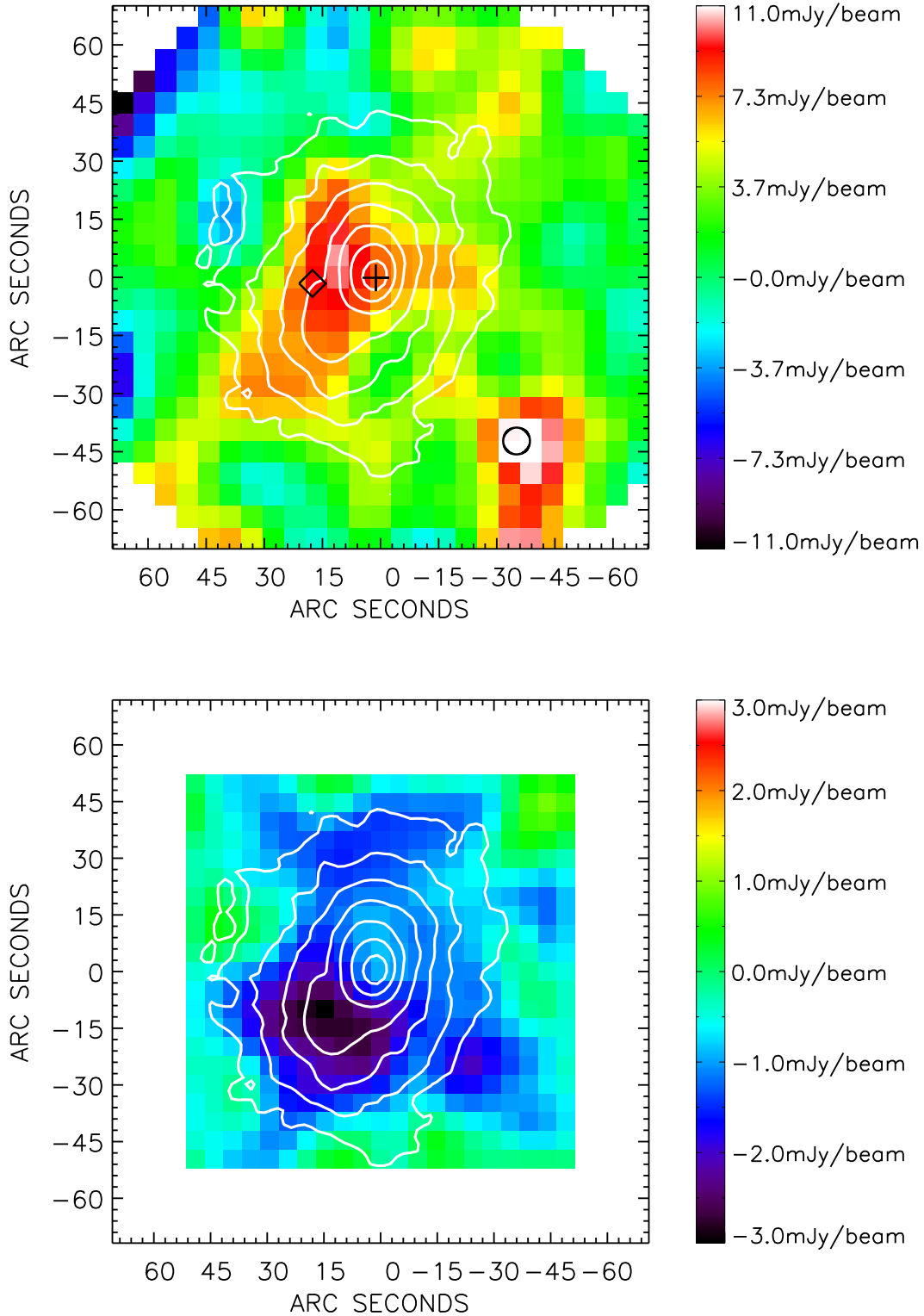


**Fig. 1.** SZE increment and decrement images of RX J1347–1145 at 350 GHz (top) and 150 GHz (bottom), respectively. Both images are centered at  $13^{\text{h}}47^{\text{m}}30^{\text{s}}.54 - 11^{\circ}45'09''.4$  (J2000) and smoothed with a  $15''$  Gaussian filter. The rms levels measured on these smoothed images are  $3.0 \text{ mJy beam}^{-1}$  and  $0.7 \text{ mJy beam}^{-1}$  at 350 GHz and 150 GHz, respectively. The positions of three sources in the field-of-view are marked by a cross (central cD), a diamond (secondary cD), and a circle (newly-discovered submillimeter source). Their contributions are not corrected in the images, but the pixels containing the sources are excised in the analysis. Contours indicate the 0.5–7.0 keV X-ray surface brightness taken by Chandra, corresponding to 64, 32, 16, 8, 4, 2, and 1% of the peak value.

$6'.0 \times 6'.0$ . The capability of this telescope for SZE observations has also been demonstrated for several other clusters at 21, 36, and 43 GHz (Tsuboi et al. 1998, 2002; Pointecouteau et al. 2002).

#### 2.4. Radio Sources

Radio sources can be serious contamination against measurements of the SZE (e.g., Cooray et al. 1998). In our analysis, we excise pixels that are potentially contaminated by radio sources. There are in total three sources in our observing field; one known radio source, one newly-discovered submillimeter source, and one candidate source. We briefly describe their properties below.

At the center of our target cluster, there is a known radio source whose flux has been measured at several frequencies (Komatsu et al. 1999, 2001; Pointecouteau et al. 2001). This source is the central cD galaxy, and the optical spectroscopy implies that it hosts an AGN with a very strong OII emission line (Schindler et al. 1995; Cohen, Kneib 2002). The spectrum in radio bands continues to decline with frequency, implying synchrotron emission from the AGN. The flux measured by VLA at 22.46 GHz is  $11.55 \pm 0.17$  mJy (Komatsu et al. 2001). A power-law extrapolation of the lower frequency measurements implies  $4.3 \pm 0.3$  mJy and  $2.7 \pm 0.4$  mJy at 150 GHz and 350 GHz, respectively.

We have also found a bright submillimeter source in our SCUBA image (figure 1), located at  $\sim 60''$  southwest from the cluster center. The flux at 350 GHz is  $15.4 \pm 5.3$  mJy. The existence of the source has been confirmed by our VLA follow-up observations at 8.46 GHz. This newly-discovered submillimeter source merits further investigation, and the results will be reported elsewhere (I. Tanaka et al. in preparation).

The secondary cD galaxy located at  $18''$  east of the cluster center (Schindler et al. 1995) may also contaminate our 350 GHz image. The optical spectroscopy implies that this source is a red elliptical galaxy with no OII emission line, and has a comparable *R*-band luminosity to the central cD (Schindler et al. 1995; Cohen, Kneib 2002). No radio counterpart has been detected between 1.4 GHz and 150 GHz, suggesting that this source does not host an AGN. In our 350 GHz image, an enhanced emission is indicated around the position of the secondary cD. This emission may originate from dust in the source and it needs to be confirmed by infrared observations. Though this source is not responsible for all of the extended emission seen in the map, it may distort the image. To be conservative, we exclude the pixels around this galaxy in our analysis.

#### 2.5. SZE Increment and Decrement Images

Figure 1 shows high-resolution SZE increment and decrement images we obtained at 350 GHz and 150 GHz, respectively. Both images are centered at  $13^{\text{h}}47^{\text{m}}30^{\text{s}}.54 - 11^{\circ}45'09''.4$  (J2000). For display purposes, they are smoothed by a Gaussian filter with an FWHM of  $15''$ , while the intensities are still given per beam-sizes listed in

table 1.<sup>1</sup> The rms levels measured on these *smoothed* images are  $3.0$  mJy beam<sup>-1</sup> and  $0.7$  mJy beam<sup>-1</sup> at 350 GHz and 150 GHz, respectively. The contributions of the three sources described in subsection 2.4 are explicitly shown. The zero level is defined by the average intensity at the map edge. Overlaid are the contours of 0.5–7.0 keV X-ray surface brightness taken by Chandra.

As first discovered by Komatsu et al. (2001), the SZE decrement at 150 GHz shows a clear enhancement at  $\sim 20''$  southeast from the X-ray center of this cluster. The significance of the southeast peak in the 150 GHz image is at the  $4.2\text{-}\sigma$  level, strongly indicating that there is a substructure in this region. The position of the peak is in good agreement with that of the enhanced X-ray emission found by Chandra (Allen et al. 2002). The increment image at 350 GHz also shows a similar extended feature in the southeast region, while a higher noise level and possible contamination from the secondary cD make it harder to identify the excess emission by eye.

Although the S/N of the present data is not sufficient for a detailed pixel-to-pixel confrontation, a quantitative comparison is still possible by means of azimuthally averaged surface brightness profiles. We divide the 350 GHz and 150 GHz maps into four quadrants as in figure 2 of Komatsu et al. (2001): southeast (SE), southwest (SW), northeast (NE) and northwest (NW). Figure 2 displays radial profiles in these quadrants after excluding the pixels within a radius of  $10''$  from the three radio sources described in subsection 2.4. The radial bins are as listed in table 1. To eliminate ambiguities in their absolute values (e.g., by the sky noise), the SZE signals relative to the map edge are used in our analysis. More specifically, the zero level of the radial profile data is fixed by the average intensity in the outermost bins in the SW, NE, and NW quadrants. The error associated with this zero-level correction is included in the error assigned to each radial bin.

The detected signals in all the four quadrants in figure 2 show extended increment and decrement features characteristic of the SZE at 350 GHz and 150 GHz, respectively. The signals in the SE quadrant between radii  $10''$  and  $50''$  are systematically higher than those in the other directions in both bands. Those in the other directions are on the whole consistent with one another. Only the  $40'' - 50''$  bin in the NE quadrant at 350 GHz deviates from the data in the other directions at the  $2.5\text{-}\sigma$  level. This may partly be due to a reference (negative) signal of the 15 mJy source in the SW region as a result of the  $120''$  chopping, yet it should diminish below the current noise level by a sky rotation. We have checked that our results are insensitive to the presence of this particular bin.

As noted by Allen et al. (2002), the X-ray surface brightness profile is also regular except for the SE quad-

<sup>1</sup> The definition of the intensity after smoothing is different from that in figure 1 of Komatsu et al. (2001), which was recalibrated to the intensity per beam-size of  $20''.6$  (an effective beam-size of the smoothed image at 150 GHz). The significance levels are identical in both cases. All scientific analyses are done on raw maps before smoothing and not affected by the above difference.

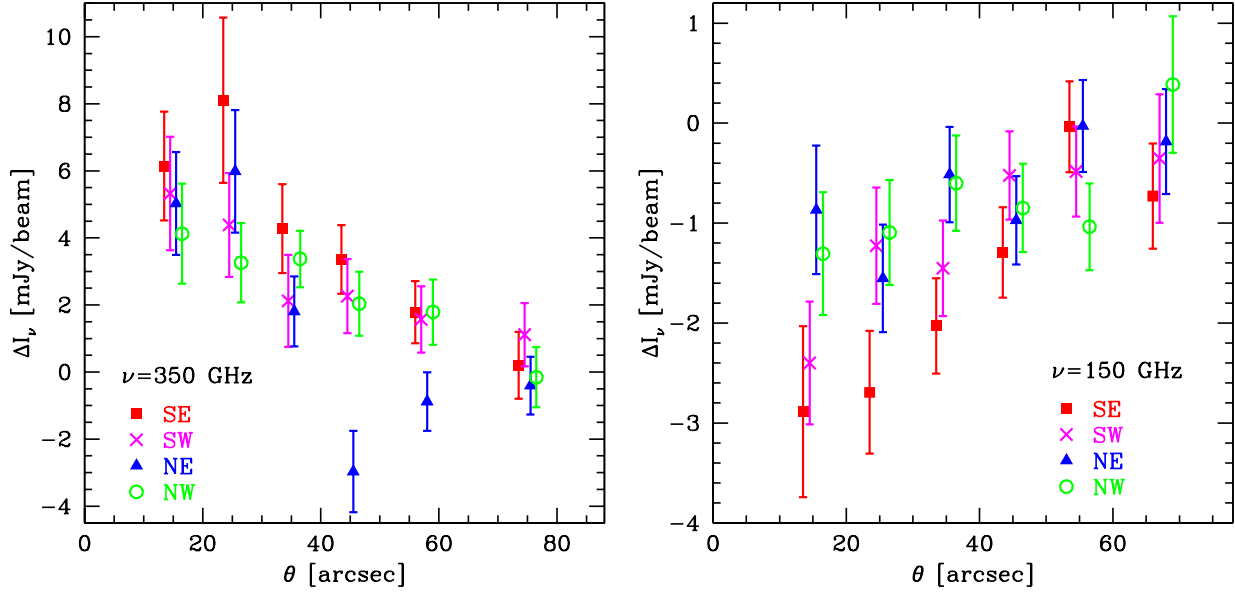


**Fig. 2.** Radial surface brightness profiles at 350 GHz (left) and 150 GHz (right) in the four quadrants; SE (filled squares), SW (crosses), NE (filled triangles), and NW (open circles). The pixels within a radius of  $10''$  from three point sources are excluded. The zero level is fixed by the average intensity in the outermost bins other than the SE quadrant. For clarity, the radial positions are slightly shifted and horizontal error bars are omitted.

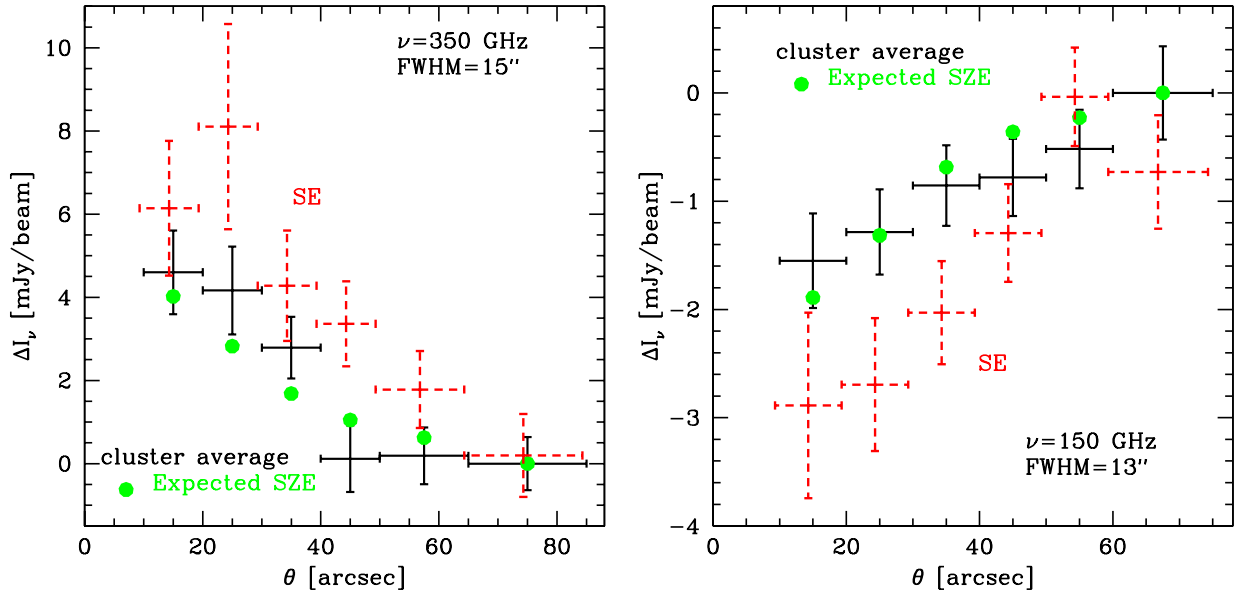


**Fig. 3.** Same as figure 2 except for showing the cluster average component (solid error bars) and of the SE quadrant (dashed error bars). Filled circles indicate the SZE signals expected for the cluster average component from Chandra X-ray imaging and spectroscopy in the case of spherical gas distribution and zero peculiar velocity (see section 3 for details).

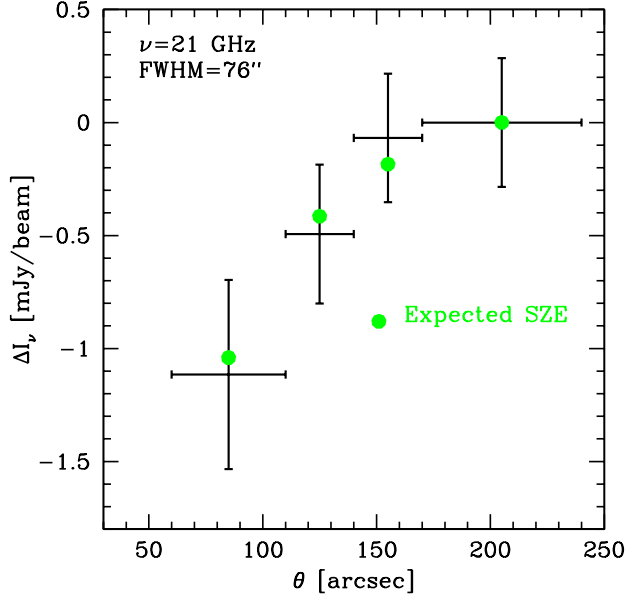


**Fig. 4.** Radial surface brightness profile at 21 GHz after subtraction of the central radio source. The pixels within a radius of  $85''$  from the center of the excess SZE in the SE region are also excluded. The zero level is determined by the intensity in the outermost bin. Filled circles indicate the SZE signals expected from Chandra X-ray imaging and spectroscopy in the case of spherical gas distribution and zero peculiar velocity (see section 3 for details).

rant. In the rest of this paper, we combine the NW, NE, and SW quadrants and refer to them as the “cluster average component”. Figure 3 illustrates that the radial surface brightness profiles of the cluster average component at 350 GHz and 150 GHz are both consistent with those expected from Chandra X-ray imaging and spectroscopy of the same region (see section 3 for details). The difference between the signals in the SE quadrant and the cluster average peaks at  $\theta \sim 25''$ .

Figure 4 shows the radial surface brightness profile of the 21 GHz data. The zero level is determined by the intensity in the outermost bin. The central source contribution was subtracted using a direct measurement ( $11.55 \pm 0.17$  mJy) at 22.46 GHz. Because of the wide beam-size, we do not treat the SE quadrant separately for the 21 GHz data. We instead have excluded the pixels within a radius of  $85''$  from the center of the SE excess indicated in the 150 GHz image. Consequently the 21 GHz data within  $60''$  from the cluster center are not used in the analysis. The extended decrement in figure 4 is also consistent with that expected from the Chandra observation for the cluster average component.

In summary, we use the radial profile data at 350 GHz, 150 GHz, and 21 GHz presented in figures 3 and 4. At 350 GHz and 150 GHz, we exclude the pixels within a radius of  $10''$  from the three radio sources described in subsection 2.4 and treat the SE quadrant separately from the other directions. At 21 GHz, we excise the pixels within a radius of  $85''$  from the center of the SE excess.

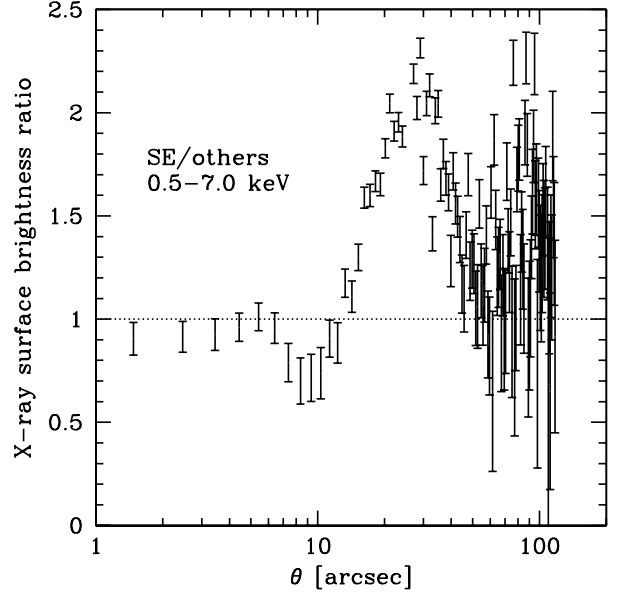


**Fig. 5.** Ratio of the 0.5–7.0 keV surface brightness in the SE quadrant and the other directions. The dotted line corresponds to an isotropic profile.

In all cases, we measure the intensity differences relative to the outermost bin.

## 2.6. X-Ray Imaging and Spectroscopy with Chandra

Allen et al. (2002) present their Chandra ACIS observations of RX J1347–1145. They found an excess X-ray emission at a position consistent with the SZE enhancement and unambiguously confirmed the presence of the substructure reported in Komatsu et al. (2001). Using the 0.5–7.0 keV band spectra, they determined the emission-weighted temperature of the SE quadrant between radii  $8''.8$  and  $28''.6$  as being  $kT_e = 18.0^{+2.7}_{-2.3}$  keV. This is significantly higher than the temperature  $kT_e = 12.7 \pm 1.0$  keV of the same radial bin in other directions. When the SE quadrant is removed, the X-ray emission appears to be smooth; the mean temperature is  $kT_e = 12.0^{+0.62}_{-0.59}$  keV and the mean metallicity is  $Z = 0.41 \pm 0.07 Z_\odot$  in the  $0'' - 108''.2$  region. The X-ray spectra indicate clear evidence of a temperature gradient (figures 4 and 5 of Allen et al. 2002) and marginal evidence for a metallicity gradient.

We use essentially the same Chandra ACIS-S3 data in the 0.5–7.0 keV band as Allen et al. (2002). The surface brightness contours are overlaid in figure 1. The imaging data have been flat-fielded by correcting the effective area of the telescope and detector with the exposure map. The background subtraction was performed using an on-chip background region, located at  $\sim 4' - 5'$  from the cluster center. We further plot in figure 5 the ratio of the counts in the SE quadrant and the cluster average component. The bin size is  $0''.984$ , corresponding to two detector pixels. The excess emission has a prominent peak at  $\theta \sim 25''$  with very high significance, which coincides with the location

of the excess SZE.<sup>2</sup>

### 3. Combined Analysis on the Cluster Average Component

We first focus on the global properties of RX J1347–1145, excluding the SE quadrant. The projected SZE and X-ray data for the cluster average component both appear to be smooth. We thus model this component as a spheroid with an axis ratio of  $1 : 1 : \eta$ , where  $\eta$  is an elongation factor in the line-of-sight direction.

#### 3.1. Modeling the X-Ray Surface Brightness

In modeling the X-ray imaging data, we compute the volume emissivity of a fully ionized plasma with SPEX ver 1.10 (Kaastra et al. 1996).<sup>3</sup> We fix the absorbing hydrogen column density at the nominal Galactic value,  $N_{\text{H}} = 4.85 \times 10^{20} \text{ cm}^{-2}$  (Dickey, Lockman 1990), metallicity at its global mean for the cluster average component,  $Z = 0.41 Z_{\odot}$  (Allen et al. 2002), and the ratio of electron and hydrogen numbers at  $n_e/n_{\text{H}} = 1.20$  (Feldman 1992). The model X-ray surface brightness is then given through a line-of-sight integral of the emissivity, using electron temperature and density profiles described below.

We assume that the electron temperature at position  $(\theta, \phi)$  in the cluster is given by an axi-symmetric model along the line-of-sight:

$$T_e(\theta, \phi) = T_e^{\text{sph}} \left[ \sqrt{\theta^2 + (\phi/\eta)^2} \right], \quad (1)$$

where  $\theta$  is an angular radius on the sky,  $\phi$  is the corresponding size in the line-of-sight direction, and  $T_e^{\text{sph}}$  is the temperature deprojected assuming  $\eta = 1$ . Unless otherwise stated, we adopt for  $T_e^{\text{sph}}$  the temperature profile data from the spectral deprojection analysis presented in figure 5 of Allen et al. (2002). They are also plotted for reference in figure 8 and given in eight radial bins at 0–3.5, 3.5–7.4, 7.4–14.2, 14.2–21.5, 21.5–36.0, 36.0–50.7, 50.7–72.2, and 72.2–108.2 arcsec.

The electron density profile is correspondingly approximated by a beta-model:

$$n_e(\theta, \phi) = n_{e0} \left[ 1 + \frac{\theta^2 + (\phi/\eta)^2}{\theta_c^2} \right]^{-3\beta/2}, \quad (2)$$

where the central density  $n_{e0}$ , the angular core radius  $\theta_c$ , the slope parameter  $\beta$ , and  $\eta$  are free parameters. The outer boundary of the cluster is taken at  $\sqrt{\theta^2 + (\phi/\eta)^2} = \theta_{\text{vir}}$ , where  $\theta_{\text{vir}} = 350''$  is the angular size corresponding to the virial radius, 2.0 Mpc, of this cluster (Allen et al. 2002). As the X-ray temperature profile data are available only within an angular radius of  $108''$ , we use the temperature in the outermost bin for the regions beyond

that. The results of our analysis are insensitive to a specific choice of the boundary, because the X-ray emission declines rapidly at the envelope (and the signal relative to the map edge is used for the SZE).

We fit the X-ray surface brightness data between radii  $4''.9$  and  $108''.2$  with a bin size of  $0''.984$ , excluding the SE quadrant. The model surface brightness from equations (1) and (2) is averaged over each radial bin, neglecting the convolution with the detector point spread function. We then obtain

$$n_{e0} \eta^{1/2} = 0.128_{-0.013}^{+0.014} \text{ cm}^{-3}, \quad (3)$$

$$\theta_c = 7''.37_{-0.62}^{+0.71}, \quad (4)$$

$$\beta = 0.583_{-0.012}^{+0.012}, \quad (5)$$

with  $\chi^2 = 118$  for 102 degrees of freedom (d.o.f.). The data at  $\theta < 4''.9$  show an excess over a simple beta-model profile; a fit including them yields  $\chi^2/\text{d.o.f.} = 250/107$ . This departure is irrelevant to modeling the SZE data at  $\theta > 10''$  in the present analysis. We attempt to break the degeneracy between  $n_{e0}$  and  $\eta$  using the SZE data in subsection 3.3.

In determining the errors quoted in the above equations, we took into account the errors in the adopted temperature profile and metallicity as follows. First, the mean values of the beta-model parameters were determined using the mean values of the temperature in each radial bin and metallicity. Second, temperatures were varied randomly within their  $1\text{-}\sigma$  errors in each radial bin. The metallicity was also varied within its  $1\text{-}\sigma$  error,  $\pm 0.17 Z_{\odot}$ , to which we assigned the variance of the radially binned metallicities (table 4 of Allen et al. 2002), assuming that they are distributed randomly around the global mean  $Z = 0.41 Z_{\odot}$ . For a given set of such temperatures and metallicity, we drew a confidence region ellipsoid in the  $(n_{e0}\eta^{1/2}, \theta_c, \beta)$  space. Third, the same procedure was repeated for different sets of temperatures and metallicity. The errors of the beta-model parameters were determined by the ‘‘envelope’’ of all the confidence-region ellipsoids. Since correlation of temperatures between different radial bins or with metallicity was neglected, the derived errors should be regarded as upper limits on their true values.

#### 3.2. Modeling the SZE Surface Brightness

We adopt the same electron temperature and density profiles as equations (1) and (2) to model the SZE. Also incorporating the line-of-sight peculiar velocity,  $V_{\text{p}}$ , of a cluster, the SZE intensity at angular radius  $\theta$  and frequency  $\nu$  is computed as

$$I_{\nu}(\theta) = 2i_0 d_A(z) \int_0^{\phi_{\text{max}}} \left\{ p(x) \left[ \frac{kT_e(\theta, \phi)}{m_e c^2} \right] \sigma_{\text{T}} n_e(\theta, \phi) + q(x) \left( \frac{V_{\text{p}}}{c} \right) \sigma_{\text{T}} n_e(\theta, \phi) + C_{\text{R}}(x, n_e, T_e, V_{\text{p}}) \right\} d\phi, \quad (6)$$

where

$$p(x) = [x \coth(x/2) - 4] q(x), \quad (7)$$

$$q(x) = x^4 e^x / (e^x - 1)^2, \quad (8)$$

<sup>2</sup> The ratios of the counts at the SE peak position to those of the background are 110 and 16829 for ROSAT HRI (0.2–2 keV) and Chandra ACIS-S3 (0.5–2 keV), respectively. The significant improvement in the S/N in Chandra observations turns out to be crucial for the unambiguous detection of the SE excess, which was not prominent in the ROSAT HRI image of Schindler et al. (1997).

<sup>3</sup> Information available at <http://www.sron.nl/divisions/hea/spex/>.



and  $x = h_P \nu / (k T_{\text{CMB}})$ ,  $i_0 = 2(k T_{\text{CMB}})^3 / (h_P c)^2$ ,  $d_A(z)$  is the angular diameter distance to the cluster redshift  $z$ ,  $T_{\text{CMB}}$  is the CMB temperature,  $h_P$  is the Planck constant,  $m_e$  is the electron mass,  $\sigma_T$  is the Thomson cross section,  $c$  is the speed of light, and  $\phi_{\text{max}} = \eta \sqrt{\theta_{\text{vir}}^2 - \theta^2}$ . The first term in the integral of equation (6) corresponds to the thermal SZE, the second term to the kinematic SZE, and the last term to their relativistic corrections. We adopt the correction factor  $C_R$  given in Nozawa et al. (1998) and Itoh et al. (2003), applicable to electron temperatures up to  $\sim 50$  keV. The peculiar velocity  $V_p$  is defined to be positive if the cluster is moving toward us.

To take into account the finite spatial resolution of our detectors, the SZE intensity in equation (6) is convolved with a Gaussian beam;

$$I_\nu^{\text{conv}}(\theta) = \frac{1}{2\pi\sigma_{\text{beam}}^2} \int I_\nu(\theta') \exp\left[-\frac{(\theta' - \theta)^2}{2\sigma_{\text{beam}}^2}\right] d^2\theta', \quad (9)$$

where  $\sigma_{\text{beam}} = \text{FWHM} / \sqrt{8\ln 2}$  specifies the beam-size. The convolved intensity,  $I_\nu^{\text{conv}}(\theta)$ , is then averaged over a given radial bin to calculate the SZE surface brightness profile. Geometrical shapes of the observed field (squares at 150 GHz and 21 GHz) are taken into account at the map edge. The zero level of the model profile is defined in the same way as the observed data.

In figures 3 and 4, we have plotted the SZE surface brightness profiles expected from Chandra X-ray imaging and spectroscopy in the case of  $\eta = 1$  and  $V_p = 0$ . The expected SZE signals for the cluster average component are as a whole consistent with the observed data in all three bands.

### 3.3. Elongation Factor and Peculiar Velocity

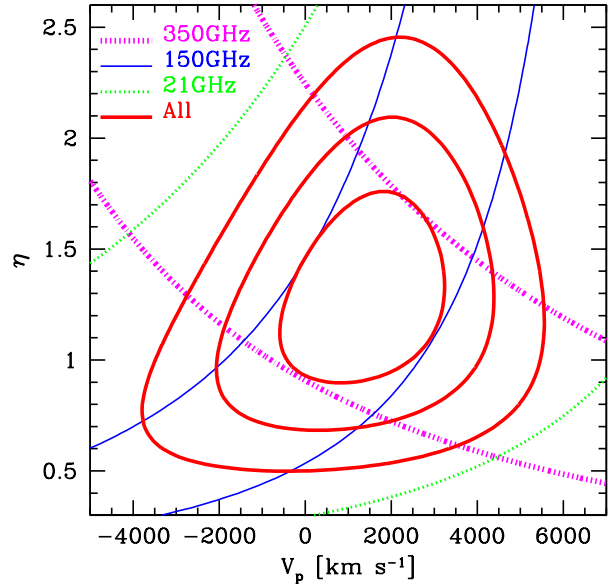
Combining the X-ray and SZE data, one can directly probe the line-of-sight elongation of a cluster. Multi-band data of the SZE also give a measure of the cluster bulk motion via the difference between the spectral shapes of the thermal and kinematic SZE [eqs (7) and (8)].

Figure 6 shows the constraints on the elongation factor  $\eta$  and a peculiar velocity  $V_p$  from the SZE data at 21, 150, and 350 GHz. The beta-model parameters are held fixed at their best-fit values given in equations (3), (4), and (5). The confidence contours derived from the SZE decrement data (21 and 150 GHz) are orthogonal to those from the increment data (350 GHz). The combination of both is therefore essential in deriving stringent constraints on the parameters. The best-fit values from the joint fit to the data in three bands are

$$\eta = 1.30_{-0.26}^{+0.29}, \quad (10)$$

$$V_p = 1420_{-1270}^{+1170} \text{ km s}^{-1}, \quad (11)$$

where  $\chi^2/\text{d.o.f.} = 7.3/11$  and the quoted errors correspond to  $\Delta\chi^2 = 1.0$  (68.3% confidence level for a single parameter of interest). Given rather large errors, there is only weak indication for elongation along the line-of-sight or positive bulk velocity of the cluster. The inferred central  $y$ -parameter is  $y_0 = 9.0 \times 10^{-4} \eta^{1/2} \simeq 1.0 \times 10^{-3}$ . Note that this is an extrapolated value from the data at  $\theta > 10''$ .



**Fig. 6.** Constraints on the elongation factor  $\eta$  and peculiar velocity  $V_p$  for the cluster average component excluding the SE quadrant. The thick solid contours indicate the 68.3, 95.4, and 99.7% ( $\Delta\chi^2 = 2.3, 6.2,$  and  $11.8$  for two parameters of interest) confidence regions from a joint fit to the data in the three bands. The other contours show the 68.3% confidence region from each of the 350 GHz (thick dotted), 150 GHz (thin solid), and 21 GHz (thin dotted) data separately.

Alternatively, one may assume that the cluster is spherically symmetric and interpret  $\eta$  as being a correction factor for the distance scale; the angular diameter distance to the cluster,  $d_A(z)$ , is longer, or equivalently, the Hubble parameter  $h$  is smaller, by a factor of  $\eta$  than adopted here ( $h = 0.71/\eta$ ).

In order to check the consistency of the shape of the SZE and X-ray surface brightness profiles more quantitatively, we plot in figure 7 the limits on  $\theta_c$  and  $\beta$  from fitting our SZE data at 21, 150 and 350 GHz. The other parameters  $n_{e0}$ ,  $\eta$  and  $V_p$  are fixed at their mean values [eqs (3), (10), and (11)]. The 21 GHz data yield the weakest constraints on  $\theta_c$  because only the data at  $\theta > 60''$  are used. The best-fit values from a joint fit to the data in the three bands are

$$\theta_c = 7''.43_{-1.96}^{+2.12}, \quad (12)$$

$$\beta = 0.588_{-0.090}^{+0.114}, \quad (13)$$

where  $\chi^2/\text{d.o.f.} = 7.2/11$  and the quoted errors correspond to  $\Delta\chi^2 = 1.0$ . The quantitative agreement with the X-ray results further ensures that the electron density profile of the cluster excluding the SE quadrant and the central  $\sim 10''$  is well approximated by the beta-model.

If we adopt a simplified isothermal model with the emission-weighted temperature  $kT_e = 12.0_{-0.59}^{+0.62}$  keV, a fit to the X-ray surface brightness profile between radii  $4''.9$  and  $108''.2$  yields  $n_{e0} \eta^{1/2} = 0.135 \pm 0.008 \text{ cm}^{-3}$ ,  $\theta_c = 7''.01 \pm 0.27$ , and  $\beta = 0.580 \pm 0.004$ , with  $\chi^2/\text{d.o.f.} = 115/102$ . The errors include those in the assumed tem-

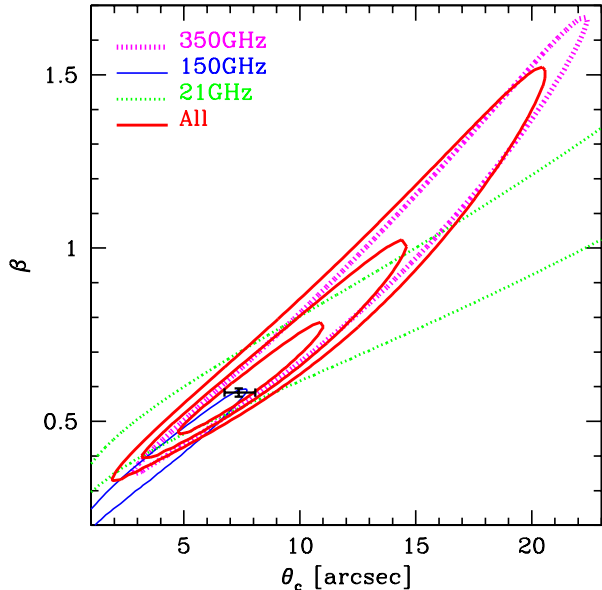


**Fig. 7.** Constraints on the beta-model parameters  $\theta_c$  and  $\beta$  for the cluster average component excluding the SE quadrant. The meanings of the contours are the same as in figure 6. The error bars are the limits from the X-ray surface brightness data by Chandra given in equations (4) and (5).

perature and metallicity as described in subsection 3.1. The above beta-model parameters are still consistent with equations (3), (4), and (5) within  $1\text{-}\sigma$  errors. The fitted values for  $\eta$  and  $V_p$  in the isothermal model are  $\eta = 2.28^{+0.52}_{-0.47}$  and  $V_p = 1020^{+830}_{-920}$  km s $^{-1}$ , respectively, with  $\chi^2/\text{d.o.f.} = 8.9/11$ . A comparison with the value in our detailed model [eq. (10)] indicates the importance of the temperature profile in determining the Hubble constant by the SZE (Inagaki et al. 1995). The fact that the isothermal approximation in this cluster overestimates  $\eta$  (i.e., underestimates the Hubble constant) is consistent with the finding of Schmidt, Allen, and Fabian (2003).

### 3.4. Temperature Deprojection

With the current X-ray spectrometers, it is still difficult to determine reliably the temperature of gas well above 10 keV. It is also likely that spatially resolved X-ray spectroscopy is unavailable for a sample of distant clusters targeted for in the future SZE surveys. We thus explore a new possibility of constraining the temperature structure of clusters solely by imaging observations.

By fitting simultaneously the surface brightness profiles of the SZE ( $\propto \int n_e T_e dl$ ) and X-rays ( $\propto \int n_e^2 T_e^{1/2} dl$ ), one can in principle determine the radial electron density and temperature profiles of a cluster. We fit the radial profile data at 150 GHz, 350 GHz and 0.5–7.0 keV of RX J1347–1145 with the following set of free parameters:  $n_e$ ,  $\theta_c$ ,  $\beta$ , and temperatures in five radial bins 10–20, 20–30, 30–40, 40–60, and 60–80 arcsec. Neglecting for a moment the knowledge of spatially resolved spectroscopy, the temperature in other parts of the cluster is fixed at its global

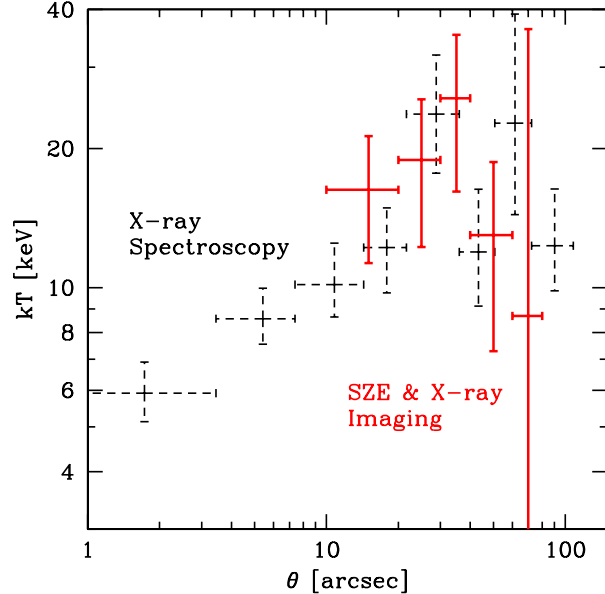


**Fig. 8.** Deprojected temperatures from a combination of the SZE and X-ray imaging data (solid error bars), independent of spatially resolved X-ray spectroscopy. Also plotted for reference are the deprojected temperatures from the Chandra X-ray spectroscopy used in subsections 3.1–3.3 (dashed error bars, Allen et al. 2002).

mean,  $kT_e = 12.0$  keV. Given the quality of the present data, we assume  $\eta = 1$  and  $V_p = 0$  for simplicity.

Figure 8 compares the deprojected temperatures in the current method and the X-ray spectral analysis of Allen et al. (2002). With the present set of multi-wavelength imaging data, we are able to constrain the radial temperature profile between 10'' and 60'', which is indeed consistent with the results of the Chandra X-ray spectroscopy. The fitted values of the other parameters are  $n_e = 0.130 \pm 0.006$  cm $^{-3}$ ,  $\theta_c = 7''.34 \pm 0.31$ ,  $\beta = 0.585 \pm 0.005$  with  $\chi^2/\text{d.o.f.} = 121/107$ , in good agreement with equations (3), (4), and (5).

## 4. Combined Analysis on the High Temperature Substructure

A combination of high-resolution SZE and X-ray images further provides a unique diagnosis of internal structures of galaxy clusters. We apply this method to the southeast excess component of RX J1347–1145 and determine its mean temperature, gas density, and the extent along the line-of-sight as follows. The X-ray and SZE signals are modeled in the same way as in section 3, except that the beta-model density profile and the temperature profile [eqs (1) and (2)] are not relevant in this section.

First, we assume that the excess component is embedded in the ambient gas identical to that in the other directions of the cluster, i.e., background and foreground components are approximated by the cluster average component. The signals due to the excess are then given by the differences in the surface brightness between the SE

quadrant and the cluster average component at 150 GHz, 350 GHz, and 0.5–7.0 keV. We take the difference at  $\theta = 10'' - 28''.6$ , where the enhancement is most evident in both the SZE and X-ray images. Second, the spectroscopic temperature in this region  $18.0^{+2.7}_{-2.3}$  keV (Allen et al. 2002) is regarded as an average temperature, weighted by the detected X-ray count rates, of the excess component and the ambient gas. For the latter, we assign the temperature of the cluster average component at the same radius,  $12.7 \pm 1.0$  keV. Third, we assume that the excess gas is distributed uniformly (like a cylinder) over the physical length  $L_{\text{ex}}$  along the line-of-sight with electron density  $n_{\text{ex}}$  and temperature  $T_{\text{ex}}$ . We fiducially fix the line-of-sight peculiar velocity of the excess gas at the mean value in equation (11).

From the excess signals at 150 GHz, 350 GHz, and 0.5–7.0 keV, and of the X-ray emission weighted temperature, we obtain:

$$kT_{\text{ex}} = 28.5 \pm 7.3 \text{ keV}, \quad (14)$$

$$n_{\text{ex}} = (1.49 \pm 0.59) \times 10^{-2} \text{ cm}^{-3}, \quad (15)$$

$$L_{\text{ex}} = 240 \pm 183 \text{ kpc}, \quad (16)$$

corresponding to the mean  $y$ -parameter of  $4.1 \times 10^{-4}$ . Including the line-of-sight velocity as an additional free parameter gives only a weak constraint,  $V_{\text{ex}} = 790 \pm 6880 \text{ km s}^{-1}$ , while the other parameters are essentially unchanged:  $kT_{\text{ex}} = 28.4 \pm 7.4 \text{ keV}$ ,  $n_{\text{ex}} = (1.53 \pm 0.73) \times 10^{-2} \text{ cm}^{-3}$ , and  $L_{\text{ex}} = 229 \pm 213 \text{ kpc}$ . Alternatively, by fitting only the surface brightness differences, without any knowledge of the X-ray emission-weighted temperature, the results are  $kT_{\text{ex}} = 33.4 \pm 56.9 \text{ keV}$ ,  $n_{\text{ex}} = (1.75 \pm 2.76) \times 10^{-2} \text{ cm}^{-3}$ , and  $L_{\text{ex}} = 179 \pm 543 \text{ kpc}$ . While the errors are still large, the latter fit indicates a further possibility of constraining the gas temperature via the relativistic correction of the SZE once the data attain better precision. Equations (15) and (16), together with the projected area of the SE substructure on the sky,  $560 \text{ arcsec}^2$ , give the total gas mass of  $M_{\text{gas}} \sim 2 \times 10^{12} M_{\odot}$  for the excess component.

We have also attempted to constrain the temperature of this excess component directly with the Chandra X-ray spectra. We first fit the 0.5–7.0 keV spectrum of the cluster average component between radii  $8''.8$  and  $28''.6$  with the MEKAL thin-thermal plasma model (Mewe et al. 1985, 1986; Kaastra 1992; Liedahl et al. 1995) to obtain  $kT_{\text{e}} = 12.6^{+1.2}_{-1.0} \text{ keV}$ , a value consistent with that reported in Allen et al. (2002). We then fit the spectrum of the SE quadrant of the same radii with a two-component MEKAL model, incorporating both the cluster average with 12.6 keV (fixed) and the excess. The amplitude of the former component was reduced by a geometrical factor of 3. Though weak, the derived limit on the temperature of the latter component,  $kT_{\text{ex}} > 21.5 \text{ keV}$  at the 90% confidence level, is fully consistent with equation (14).

## 5. Discussion

The presence of very high temperature gas in excess of 20 keV inferred in section 4 supports strongly an idea that the cluster has undergone a recent subcluster merger (Cohen, Kneib 2002; Allen et al. 2002). We explore the properties of this region based on a simple one-dimensional shock model as follows.

We assume that the pre-shock gas has the density  $n_1$  and the temperature  $kT_1 = 12.7 \text{ keV}$  expected for the cluster average component. Given a steep density gradient and an uncertainty in the subclump position along the line-of-sight,  $n_1$  is regarded as being yet undetermined. The post-shock gas is assumed to have  $n_2 = 1.49 \times 10^{-2} \text{ cm}^{-3}$  and  $kT_2 = 28.5 \text{ keV}$  from equations (14) and (15). Applying the Rankine–Hugoniot conditions across the shock with an adiabatic index  $\gamma = 5/3$ , we find that the Mach number of the pre-shock gas is  $\mathcal{M}_1 = 2.1$ , and the velocity of the pre-shock and post-shock gas relative to the shock front are  $v_1 = 3900 \text{ km s}^{-1}$  and  $v_2 = 1600 \text{ km s}^{-1}$ , respectively. For a head-on collision of equal mass clumps, the collision velocity is  $\Delta v = 2(v_1 - v_2) = 4600 \text{ km s}^{-1}$ . The corresponding density ratio  $n_2/n_1 = 2.4$  implies  $n_1 = 6.2 \times 10^{-3} \text{ cm}^{-3}$ . Assuming further that the pre-shock gas distribution is described by equations (2)–(5) with  $\eta \sim 1$ , the distance of the subclump from the cluster center, including the line-of-sight displacement, is suggested as  $\sqrt{\theta^2 + \phi^2} \sim 40''$  or 230 kpc.

Previous hydrodynamical simulations of Takizawa (1999), for instance, showed that the gas temperature can rise up to  $kT_{\text{e}} > 25 \text{ keV}$  as a result of a head-on collision of  $5 \times 10^{14} M_{\odot}$  clusters with relative velocity  $\Delta v > 4000 \text{ km s}^{-1}$ . The highest temperature gas is likely to emerge near the bounce-shock with total gas mass of  $\sim 10^{12} M_{\odot}$  for a duration of  $\sim 0.5 \text{ Gyr}$  (M. Takizawa, private communication). Gravitational softening length of 20 kpc and the gas particle mass of  $10^{10} M_{\odot}$  used in the simulations are sufficient for resolving the substructures comparable to that found in RX J1347–1145. Though it is still premature to conclude the origin of the hot gas in RX J1347–1145, these results are consistent with our interpretation of shock heating during a violent merger.

A merger event may also produce high-energy non-thermal particles. While BeppoSAX observations of RX J1347–1145 (Ettori et al. 2001) have found little evidence for their contribution to the entire X-ray emission of this cluster, nonthermal particles may affect the enhanced SZE and X-ray signals locally. We examined the Chandra spectrum of the SE excess position ( $8''.8 - 28''.6$ ), and found that the effective photon index is 1.4 without subtracting the cluster average component. This is comparable to, or even harder than, those expected from the inverse Compton and nonthermal bremsstrahlung emissions, 1.5 and 2.0, respectively, in the strong shock limit (Sarazin 1999; Sarazin, Kempner 2000). Thus, if the non-thermal component is included in the spectral analysis, the inferred thermal temperature would become higher, unless the spectrum is fully dominated by the inverse Compton emission resulting from the strong shock. A

harder nonthermal electron spectrum may be possible as a result, for instance, of Coulomb losses, but they will also lead to unacceptably large heating of the thermal gas (Petrosian 2001; Takizawa 2002). Contribution of nonthermal electrons to the SZE signals depends sensitively on the amount and spectrum of relatively low energy nonthermal electrons (e.g., Ensslin, Kaiser 2000; Colafrancesco et al. 2003), but is unlikely to dominate over the thermal SZE (Shimon, Rephaeli 2002). In any case, if the nonthermal component is separated from the thermal and kinematic SZE in future observations, it will provide a useful probe of the nature of high-energy populations in clusters.

In the present analysis, we excluded the regions around already resolved contaminating sources. One further possibility of contamination, particularly in the 350 GHz image, is unresolved emission from background submillimeter sources (Smail et al. 2002 and references therein). If such sources are distributed rather uniformly in the cluster field, their average contribution has been subtracted in our analysis, as we only used the signal relative to the map edge. Shot-noise-like signals, on the other hand, may increase the noise level of the image, but are unlikely to produce the extended feature illustrated in figure 2. The gravitational lensing effect tends to enhance the emission close to the critical lines, not toward the cluster center. We thus conclude that the contribution of the background sources is unlikely to change the main results of this paper.

Another possibility of contamination is dust emission inside the cluster. Edge et al. (1999) report detection of such emission in two out of seven central galaxies in clusters. Dust may also be present in the intracluster medium (Dwek et al. 1990; Stickel et al. 2002), although such diffuse dust is likely to be destroyed via sputtering within the age of the Universe (Draine, Salpeter 1979). Since dust emission from the cluster member galaxies or the intracluster medium will peak at far-infrared wavelengths, it can be constrained directly by infrared facilities, such as SIRTf and Astro-F. We will investigate these points in detail elsewhere (K. Yamada, T. Kitayama, in preparation). It will also be interesting to see if the secondary cD really contains dust, as implied by our SCUBA map.

## 6. Conclusions

We have performed combined analyses of the highest resolution SZE and X-ray images currently available for RX J1347–1145. The data at both 150 GHz and 350 GHz show clear signatures of enhanced SZE signals at  $\sim 150$  kpc southeast from the center of this cluster. We have separately determined the temperature, density, and the line-of-sight extent of this excess component, after removing the foreground and background signals. The presence of high-temperature gas with  $28 \pm 7$  keV strongly indicates that the cluster has recently experienced a major merger.

Excluding the regions around the southeast enhancement and the radio sources, the SZE signals at 350, 150, and 21 GHz agree well with those expected from the elec-

tron density and temperature profiles of Chandra X-ray observations. Our multi-band SZE data indicate marginal evidence for the line-of-sight elongation of the gas distribution or non-zero peculiar velocity. The central  $y$ -parameter extrapolated from radii greater than 60 kpc is  $y_0 \simeq 1.0 \times 10^{-3}$ . We further present a temperature deprojection technique using the SZE and X-ray imaging data. The radial temperature profile so obtained between 60 and 350 kpc are all consistent with those based on the X-ray spectral deprojection analysis of Allen et al. (2002).

Our results demonstrate the power of high-resolution SZE mapping observations. In particular, they provide a unique probe of the temperature structure in distant clusters for which spatially resolved X-ray spectroscopy is unavailable. With its unlimited sensitivity to high temperature, the SZE has an advantage over X-rays in detecting the gas with temperatures well above 10 keV. As demonstrated for RX J1347–1145, an angular resolution of  $\sim 10''$  is essential in resolving irregular morphology of merger-heated gas in distant clusters. Large detector arrays, such as BOLOCAM on the Large Millimeter Telescope (Glenn et al. 2003) and SCUBA-2 on the James-Clerk-Maxwell Telescope (Holland et al. 2003), will indeed be suitable for such observations. Though performed on a single cluster so far, the methodology presented in this paper will be applicable to a statistical sample of clusters obtained in the future SZE surveys.

We thank Steve Allen for providing deprojected temperature data and for useful discussions, Naoki Itoh and Satoshi Nozawa for supplying subroutines of their relativistic correction formulae, and Erik Reese, Motokazu Takizawa, Ichi Tanaka and the referee for helpful comments and discussions. NO and KY acknowledge support from Research Fellowships of the Japan Society for the Promotion of Science for Young Scientists. This work is supported in part by the Grant-in-Aid by the Ministry of Education, Culture, Sports, Science and Technology (14740133, TK).

## References

- Allen, S. W., Schmidt, R. W., & Fabian, A. C. 2002, MNRAS, 335, 256
- Bennett, C. L., et al. 2003, ApJS, 148, 1
- Birkinshaw, M. 1999, Phys. Rep. 310, 97
- Carlstrom, J. E., Holder, G. P., & Reese, E. D. 2002, ARA&A, 40, 643
- Carlstrom, J. E., Joy, M., & Grego, L. 1996, ApJ, 456, L75
- Cohen, J. G., & Kneib, J. 2002, ApJ, 573, 524
- Colafrancesco, S., Marchegiani, & P., Palladino, E. 2003, A&A, 397, 27
- Cooray, A. R., Grego, L., Holzapfel, W. L., Joy, M., & Carlstrom, J. E. 1998, AJ, 115, 1388
- Dickey, J. M., & Lockman, F. J. 1990, ARA&A, 28, 215
- Donahue, M., Gaskin, J. A., Patel, S. K., Joy, M., Clowe, D., & Hughes, J. P. 2003, astro-ph/0308024
- Draine, B. T., & Salpeter, E. E. 1979, ApJ, 231, 438
- Dwek, E., Rephaeli, Y., & Mather, J.C. 1990, ApJ, 350, 104
- Edge, A. C., Ivison, R. J., Smail, I., Blain, A. W., & Kneib J. -P. 1999, MNRAS 306, 599

- Emerson, D. T., & Gräve, R. 1988, *A&A*, 190, 353
- Ensslin, T. A., & Kaiser, C. R. 2000, *A&A*, 360, 417
- Ettori, S., Allen, S. W., & Fabian, A. C. 2001, *MNRAS*, 322, 187
- Fabian, A. C., Sanders, J. S., Allen, S. W., Crawford, C. S., Iwasawa, K., Johnstone, R. M., Schmidt, R. W., & Taylor, G. B. 2003, *MNRAS*, 344, L43
- Feldman, U. 1992, *Phys. Scr.*, 46, 202
- Glenn, J., et al. 2003, *Proc. SPIE*, 4855, ed. T. G. Phillips & J. P. Zmuidzinas, 30
- Holland, W. S., et al. 1999, *MNRAS*, 303, 659
- Holland, W. S., Duncan, W., Kelly, B. D., Irwin, K. D., Walton, A. J., Ade, P. A. R., & Robson, E. I. 2003, in *Proc. SPIE*, 4855, ed. T. G. Phillips & J. P. Zmuidzinas, 1
- Hughes, J. P., Birkinshaw, M. 1998, *ApJ*, 501, 1
- Inagaki, Y., Sugihara, T., & Suto, Y. 1995, *PASJ*, 47, 411
- Itoh, N., & Nozawa, S. 2003, *A&A*, submitted (astro-ph/0307519)
- Jenness, T., & Lightfoot, J. F. 1998, in *A.S.P. Conference Series*, 145, ed. R. Albrecht, R.N. Hook and H.A. Bushouse, 216
- Jenness, T., Lightfoot, J. F., & Holland, W. S. 1998, in *Proc. SPIE*, 3357, ed. T. G. Phillips, 548
- Jones, M., et al. 1993, *Nature*, 365, 320
- Kaastra, J. S. 1992, *An X-Ray Spectral Code for Optically Thin Plasmas* (Internal SRON-Leiden Report, updated version 2.0)
- Kaastra, J. S., Mewe, R., & Nieuwenhuijzen, H. 1996, in *UV and X-ray spectroscopy of astrophysical and laboratory plasmas*, ed. K. Yamashita and T. Watanabe, 411
- Komatsu, E., Kitayama, T., Suto, Y., Hattori, M., Kawabe, R., Matsuo, H., Schindler, S., & Yoshikawa, K. 1999, *ApJ*, 516, L1
- Komatsu, E., et al. 2001, *PASJ*, 53, 57
- Kuno, N., Matsuo, H., Mizumoto, Y., Lange, A. E., Beeman, J. W., & Haller, E. E. 1993, *Int. J. Infrared Millimeter Waves*, 14, 749
- Liedahl, D.A., Osterheld, A.L., & Goldstein, W.H. 1995, *ApJ*, 438, L115
- Markevitch, M., et al. 2000, *ApJ*, 541, 542
- Markevitch, M., Gonzalez, A. H., David, L., Vikhlinin, A., Murray, S., Forman, W., Jones, C., & Tucker, W. 2002, *ApJ*, 567, L27
- Mewe, R., Gronenschild, E. H. B. M., & van den Oord, G. H. J. 1985, *A&AS*, 62, 197
- Mewe, R., Lemen, J. R., & van den Oord, G.H.J. 1986, *A&AS*, 65, 511
- Nozawa, S., Itoh, N., & Kohyama, Y. 1998, *ApJ*, 507, 530
- Peterson, J. R., Kahn, S. M., Paerels, F. B. S., Kaastra, J. S., Tamura, T., Bleeker, J. A. M., Ferrigno, C., & Jernigan, J. G. 2003, *ApJ*, 590, 207
- Petrosian, V. 2001, *ApJ*, 557, 560
- Pointecouteau, E., Giard, M., Benoit, A., Désert, F. X., Aghanim, N., Coron, N., Lamarre, J.M. & Delabrouille, J. 1999, *ApJ*, 519, L115
- Pointecouteau, E., Giard, M., Benoit, A., Désert, F. X., Bernard J.P., Coron, N., & Lamarre, J. M. 2001, *ApJ*, 552, 42
- Pointecouteau, E., Hattori, M., Neumann, D. M., Komatsu, E., Matsuo, H., Kuno, N., & Böhringer, H. 2002, *A&A*, 387, 56
- Reese, E. D., Carlstrom, J. E., Joy, M., Mohr, J. J., Grego, L., & Holzappel, W. L. 2002, *ApJ*, 581, 53
- Rephaeli, Y. 1995, *ARA&A*, 33, 541
- Sarazin, C. L. 1999, *ApJ*, 520, 529
- Sarazin, C. L., & Kempner, J. C. 2000, *ApJ*, 533, 73
- Schindler, S., et al. 1995, *A&A* 299, L9
- Schindler, S., Hattori, M., Neumann, D. M., & Böhringer, H. 1997, *A&A* 317, 646
- Schmidt, R. W., Allen, S. W., & Fabian, A. C. 2003, *MNRAS* submitted
- Shimon, M., & Rephaeli, Y. 2002, *ApJ*, 575, 12
- Smail, I., Ivison, R.J., Blain, A. W., & Kneib, J.-P. 2002, *MNRAS*, 331, 495
- Spergel, D. N., et al. 2003, *ApJS*, 148, 175
- Stickel, M., Klaas, U., Lemke, D., & Mattila, K. 2002, *A&A*, 383, 367
- Sunyaev, R. A., & Zel'dovich Ya. B. 1970, *Ap&SS*, 7, 3
- Sunyaev, R. A., & Zel'dovich Ya. B. 1972, *Comments Astrophys. Space Phys.*, 4, 173
- Takizawa, M. 1999, *ApJ*, 520, 514
- Takizawa, M. 2002, *PASJ*, 54, 363
- Tsuboi, M., Miyazaki, A., Kasuga, T., Matsuo, H., & Kuno, N. 1998, *PASJ*, 50, 169
- Tsuboi M., Miyazaki A., Kasuga T., Kuno N., Sakamoto A., & Matsuo H. 2002, *PASJ* submitted
- Yoshikawa, K., & Suto, Y. 1999, *ApJ*, 513, 549
- Zaroubi, S., Squires, G., Hoffman, Y., & Silk, J. 1998, *ApJ*, 500, L87
- Zemcov, M., Halpen, M., Borys, C., Chapman, S., Holland, W., Pierpaoli, E., & Scott, D. 2003, *MNRAS*, 346, 1179